Environmental Science Nano

Structure and energetics of hydrogen bonding networks in dilute HOD/H2O solutions confined in silica nanopores

Journal:	*Environmental Science: Nano*
Manuscript ID	EN-ART-05-2023-000291.R1
Article Type:	Paper

Structure and energetics of hydrogen bonding networks in dilute HOD/H_2O solutions confined in silica nanopores

Anastasia G. Ilgen*[1], Hasini S. Senanayake,[2] Ward H. Thompson[2], and Jeffery A. Greathouse[3]

Environmental Significance Statement

Oxide nanopores, including silica, are abundant in the environment. When water is nanoconfined by surfaces in nanopores it exhibits anomalous physico-chemical properties, compared to unconfined counterpart. As a result, interfacial reactions inside nanopores are associated with higher enthlpies, enhanced chemisorption and irreversible surface complexation reactions. Here we show that nanoconfinement strengthens hydrogen bonds in near-interfacial regions and weakens them in the nanopore volume. This finding has important implications for the chemical reactions confined inside nanopores in the environment: the chemical species residing near pore surfaces experience strong H-bonding interactions that affect reactions involving charge transfer or solvation; alternatively, for chemical species in the middle of the pore H-bonding interactions in water are weakened, leading to a decreased energetic cost of de-solvation and corresponding shifts in the equilibrium constants. Furthermore, weakened H-bond interactions in the nanopore volume could indicate a decrease in the liquid-vapor phase transition temperature, similar to the well-known decrease in the liquid-ice transition temperature. These findings pave the way for more accurate fate and transport models for chemical species in the environment, where reactive surfaces are often nanoconfined.

Structure and energetics of hydrogen bonding networks in dilute HOD/H_2O solutions confined in silica nanopores

Anastasia G. Ilgen*[1], Hasini S. Senanayake,[2] Ward H. Thompson[2], and Jeffery A. Greathouse[3]

[1] Geochemistry Department, Sandia National Laboratories, Albuquerque, New Mexico 87185, USA

[2] Department of Chemistry, University of Kansas, Lawrence, Kansas 66045, USA

[3] Nuclear Waste Disposal Research & Analysis Department, Sandia National Laboratories, Albuquerque, New Mexico 87185, USA

* Corresponding author: agilgen@sandia.gov

Abstract

Hydrogen-bonding (H-bonding) networks in liquid H_2O define its reactivity and physico-chemical properties. In nanopores, H-bonding is not easily predictable due to the competing effects on water structure from the opposing surfaces. Here we explore H-bonding under nanoconfinement in silica nanopores. We use isotopically dilute deuterated water to exclude intermolecular oscillator coupling effects, and utilize temperature-controlled Raman spectroscopy, water sorption measurements, and molecular dynamics simulations to decipher H-bonding structures and energetics. We found two opposite trends for H-bonding under nanoconfinement: in the interfacial binding layers at the silica surfaces nanoconfinement increases H-bond strength, while in the body of the nanopore H-bond strength is decreased in comparison to bulk solutions. The existence of two populations of water in nanopores could lead to the contrasting reactivity trends under nanoconfinement for the chemical species residing near pore surfaces versus those residing in the middle of the pore. In the near-interfacial regions, strong H-bonding environments affect reactions involving charge transfer and solvation; alternatively, in the middle of the pore weakened H-bonding interactions could decrease de-solvation costs and shifts equilibrium constants. The observed H-bond weakening in SiO_2 nanopore body may indicate a decrease in the H_2O liquid-vapor phase transition temperature.

Introduction

In liquid phase, H_2O dipoles arrange into 3-dimensional hydrogen bonding (H-bonding) networks, where one H_2O can interact with up to four other H_2Os donating and accepting H-bonds.[1] H-bonding in water and aqueous solutions and associated long-range interactions define water's unique physico-chemical properties and mediate all reactions taking place in aqueous solutions, including those in the living matter.[2] Scientists have long recognized that confining water at the nano-scale results in unexpected chemical behaviors, including anomalous dielectric response,[3, 4] decrease in the density and surface tension,[5, 6] increase in gas solubilities,[7] unusual charge separation and decrease in the local pH,[8] shifting phase boundaries[9] and glass phase transitions,[10] and higher apparent viscosity.[11] A question arises – is water confined in solid nanopores equivalent to interfacial water layers at solid-water interfaces? In our conceptual view nanoconfined aqueous solutions are not fully equivalent to interfacial counterparts, because electrical double layers (EDL) extending from charged solid surfaces into bulk solutions overlap inside nanopores. Progressive EDL overlap in SiO_2 nanopores with decreasing pore diameter decreases the surface charge densities.[12] The theoretical Debye length for deionized H_2O is estimated at 1000 nm at neutral pH with 10^{-7} M hydronium and hydroxide concentrations[13], and therefore in our 4 nm and 7 nm pores filled with pure HOD/H_2O, there is a significant EDL overlap. It is not known how the overlap in EDLs affects the structure of water and aqueous solutions, and the extent to which a surface impacts nanoconfined water structure is still debated.[14] We hypothesize, that in the EDL overlap regions the dipole-dipole interactions are weakened, resulting in weaker H-bonding when compared to bulk HOD/H_2O at the same pressure-temperature conditions. To test this hypothesis, here we use vibrational spectroscopy,

H_2O vapor sorption, and classical molecular dynamics (MD) simulations to characterize H-bonding environments in HOD/H_2O nanoconfined within silica (SiO_2) nanopores.

Vibrational spectroscopy is an excellent tool for assessing H-bonding networks in H_2O.[15-20] The OH stretch region shows three broad lines: (*1*) ~3635 cm^{-1}; (*2*) ~3425 cm^{-1}; and (*3*) ~3268 cm^{-1}, that are assigned to progressively stronger H-bonding environments around OH oscillators. These shifts happen because with increasing number of H-bonds an elongation of the covalent O–H bonds takes place.[21] However, the ~3268 cm^{-1} line also includes the contribution of resonant vibrational coupling—enhanced signal due to OH oscillators moving "in-phase"[16]—significantly complicating the interpretation of the OH stretch spectra. Some previous studies ignored the resonant vibrational coupling contributions, and therefore over-estimated the tetrahedral H_2O fraction (H_2O molecules with four H-bonds, simultaneously donating two and accepting two H-bonds).[6, 17, 18] To more accurately assess the characteristics of H-bonding networks in nanopores we use a dilute HOD in H_2O, where individual OD oscillators are isolated and do not suffer from resonant vibrational coupling interferences.[15, 16]

H-bonding networks in liquid water are dynamic and change with physical and chemical variables.[22] With increasing temperature in liquid water H-bonds become weaker, which is seen in the blueshift and decreased intensity of vibrational bands, and eventually break during liquid-vapor transition. Therefore, a decrease or an increase in the *average* number of instantaneous H-bonds between H_2Os in nanopores can be compared to a temperature change in bulk water, where with increasing temperature H-bonds become weaker and have higher probability of being broken. Therefore, here we examine the effect of increasing temperature in both bulk HOD/H_2O solution and in the same solution nanoconfined in SiO_2 nanopores to assess changes in H-bond structures and to calculate H-bond energetics. H-bonding networks are also sensitive to the

addition of salts: water dipoles re-orient themselves around charged aqueous species within the 1st and 2nd solvation shells.[23, 24] Furthermore, the presence of an interface (either a solid-water or an air-water) also alters H-bonding structures of adjacent water molecules, because H_2O molecules orient themselves to maximize either water-water or water-surface interactions, depending on their favorability.[25, 26] For example, in hydrophilic SiO_2 pores due to the competition between water-water and water-surface interactions the H-bonding networks are distorted up to ~ 1 nm distance from the surface where fewer H-bonds are observed, compared to bulk H_2O.[27] Interestingly, these near-interfacial H-bonds have more negative Gibbs free energy, with less frequent breaking events, while their vibrational energy is lower in comparison to bulk water.[28] In hydrophobic carbon nanotubes, there are also fewer H-bonds on average, even though H_2Os do not form H-bonds with the confining carbon surface.[22]

MD simulation is a powerful tool for determining the details of H-bonding in nanopores.[6, 17, 18, 26, 29, 30] MD simulations often show that in the diffuse EDL region, H-bonding networks can be indistinguishable from those in the bulk H_2O when "snapshots" or static images are considered;[26, 29, 30] however, the rotational freedom of H_2O molecules, and therefore, H-bonding network re-arrangement dynamics is often slower in nanopores, compared to bulk H_2O.[28, 31-33] Here we combine Raman spectroscopy, H_2O vapor sorption measurements and MD simulations to quantify the details of H-bonding structures and the energetics of H-bonds in SiO_2 nanopores with negative surface charges.

Methods

Materials

All experiments were conducted using commercially available SBA-15 series mesoporous SiO_2 (Sigma Aldrich) with a mean pore diameter of 7.0±0.3 nm and 4.4±0.1 nm,

and surface areas of 661±5 $m^2 g^{-1}$ and 580±13 $m^2 g^{-1}$, respectively.[34] Here we refer to these materials as "SiO_2 nanopores." The volume to area ratios are 1.54×10^{-9} for the 4 nm SBA-15 and 2.06×10^{-9} for the 7 nm SBA-15, resulting in the surface water to pore water volume ratio difference ~ 25 % between these materials.

H_2O vapor sorption

To assess the effect of nanoconfinement on the interactions of SiO_2 surfaces with H_2O we quantified the H_2O adsorption onto confined (SBA-15) and unconfined SiO_2 surfaces at controlled temperatures using Dynamic Vapor Sorption (DVS) Endeavor instrument. The unconfined SiO_2 was non-porous fumed silica (Sigma Aldrich) with a surface area of 192 $m^2 g^{-1}$.[35] These SiO_2 materials are equivalent, since their silanol Si–OH surface-site densities are similar: 2.3 ± 0.2 OH nm^{-2} for the 4 nm SiO_2, 1.8 ± 0.2 OH nm^{-2} for 7 nm SiO_2, and 2.2 ± 0.2 OH nm^{-2} for non-porous SiO_2.[36] All SiO_2 samples were washed in de-ionized H_2O and dried for a minimum of 48 hours in a laboratory oven at 40 °C. A 20-30 mg solid sample was transferred into aluminum sample holder, heated to 200 °C and flushed with dry N_2 gas for 48 hours prior to H_2O adsorption measurements. The relative humidity (RH) was increased from 0% to 10% in 2% increments, and sample mass was measured continuously for 2 hours at each RH step to ensure equilibrium has been reached. An adsorption isotherm for each material was measured at 25 °C (298.15 K), 30 °C (303.15 K), 35 °C (308.15 K), 40 °C (313.15 K), and 45 °C (318.15 K) to calculate enthalpy $\Delta H_{ads,}$ and entropy ΔS_{ads} values using van Hoff's equation:

$$\ln(K) = \Delta S/R - \Delta H/RT \qquad (1)$$

where K is the equilibrium constant at a given relative humidity, and R is the universal gas constant (8.314463 $J\cdot mol^{-1}\cdot K^{-1}$). We calculated Gibbs free energy ΔG_{ads} values from $\Delta H_{ads,}$ and ΔS_{ads}. First, the H_2O surface loadings were calculated in $mol(H_2O)\times m^{-2}(SiO_2)$. Then, the

equilibrium constant (K_L) was determined by fitting a Langmuir isotherm equation $\theta=(S\times K_L\times RH\%)/(1+K_L\times RH\%)$, where θ is the measured surface loading normalized by surface area and expressed in mol(H_2O)×m^{-2}(SiO_2), S is the estimated maximum surface coverage also in mol(H_2O)×m^{-2}(SiO_2), and K_L is the equilibrium constant expressed in 1/RH% units. To convert K_L to a unitless value, it was multiplied by the measured RH%. Data in the 0-10% RH range was used to ensure that monolayer coverage was not exceeded, and adsorption in theory can be described with a Langmuir model. The Langmuir model was fit to the datapoints using Igor Pro 7 software package. The slope of the lnK_L vs. 1/T line is equal to $-\Delta H_{ads}/RT$, where R is the universal gas constant, and T is temperature. Additionally, equilibrium distribution coefficients (K_d) measured at a fixed RH value were extracted from the data. These K_d values were taken at a given point in the isotherm that corresponded to the surface coverage at 10% RH, where surface coverages by H_2O are under the mono-layer coverage; the K_d values therefore have units of mol(H_2O)×m^{-2}(SiO_2). Similar to K_L, because K_d values were measured at equilibrium conditions and represent equilibrium constants at a fixed RH, the slope of the lnK_d vs. 1/T line is equal to $-\Delta H_{ads}/RT$, where R is the universal gas constant, and T is temperature.

Raman spectroscopy

Raman spectra were collected using an XploRA Plus Raman microscope (HORIBA Scientific) with a cooled CCD detector (Jobin Yvon's Synapse camera, Syncerity OE). An unpolarized laser with 532 nm emission wavelength was used for excitation with the radiation power ~100 mW at 10-100% power in conjunction with 1200 (750 nm) grating. A combination of 100 μm slit and 300 μm hole was used. An objective with 10x magnification and a numerical aperture of 0.25 was used for excitation, with the resulting laser spot diameter of 2.6 μm. Raman spectrometer calibration was performed every 24 hours, using a polished silicon wafer. Each

spectrum was collected with 3 sec exposure and averaged over 100 scans from 2000 to 4000 cm^{-1}. Given these long measurement times, time-averaged H-bond structures were assessed. Background was subtracted by fitting linear segments under individual peaks.

Raman spectra were collected in the 2000-4000 cm^{-1} range to assess OH and OD stretch modes in bulk and in nanoconfined solutions. The SiO_2 with 4 nm and 7 nm pores were saturated with isotopically dilute HOD in H_2O aqueous solutions, where 10 vol% of D_2O were mixed into de-ionized H_2O, then spiked with HPLC grade CH_3OH, so that final CH_3OH content was 4 mol %. The saturated porous SiO_2 particles were placed in a quartz crucible, excess liquid was removed using a Kimwipe, and the crucible was sealed with a glass cover slide. The crucible was placed into a Linkam THMSG600 controlled-temperature stage. The temperature was gradually increased from room temperature to 85 ºC (358 K) in 10 °C increments, and Raman spectra were taken after a 5-minute equilibration time for each temperature. The CH stretching band at 2837 cm^{-1} in CH_3OH is not affected by temperature and it was used to normalize the intensity of each collected spectrum, since OH and OD stretch intensities are temperature-dependent.[15, 37]

H-bond energy calculations

The normalization by the CH stretch intensity enabled analysis of deuterium hydrogen bond strength based on Boltzmann statistics, as was done earlier for bulk HOD/H_2O solutions.[15] The assumptions of these analyses include (*1*) a 1:1 correspondence between Raman frequency (ν) and the energy state of the H-bond of the OD oscillator; (*2*) state multiplicity independent of temperature, and therefore Raman intensity described by the Boltzmann distribution.[15] If these assumptions are correct, then a graph of $\ln[I(\nu,T)/I(\nu_0,T)]$ vs. $1/T$ should be linear, with the slope being proportional to the energy difference between the states at ν_0 and ν and the unit for slope being K. By plotting the slope values vs. Raman frequency, we obtained vibrational energy

distribution for the OD oscillator as a function of frequency. The lowest point in this distribution is indicative of the frequency that corresponds to the H-bond vibrational energy minima. Our data indeed resulted in linear plots (SI, Fig. S1), indicating that the Boltzmann analysis is valid for these systems. The initial reference frequency v_0 was chosen at 2440 cm^{-1}, consistent with the previous findings of vibrational frequency for ice-line H-bonded scatterers.[15] This frequency indeed corresponded to the energy minima for unconfined HOD/H_2O solution; however the minima shifted to 2465 cm^{-1} for nanoconfined HOD/H_2O (SI, Fig. S3); therefore for nanopores the reference frequency v_0 was chosen at 2465 cm^{-1}, which did not shift the minimum in the plots but prevented energy scale to dip below zero (SI, Fig. S3).

Molecular Dynamics Simulations

All molecular dynamics (MD) simulations were performed using the Large-scale Atomic/Molecular Massively Parallel Simulator (LAMMPS) code.[38] The charged amorphous silica slab models used in this work were generated using a melt-cleave-quench procedure.[39] Briefly, a bulk amorphous silica structure is heated to 3000 K over 1 ns to create molten silica slabs. The melting procedure is done in the *NPT* (constant number *N*, pressure *P*, and temperature *T*) ensemble. The periodic simulation cell is then expanded in the *z*-direction up to 80 Å and equilibrated for 1 ns at 3000 K in the NP_zAT (P_z is the pressure in the *z*-direction and *A* is the surface area in *xy* plane) ensemble, keeping the *x* and *y* dimensions constant at 21.0155 Å. At this point, atomistically different slabs were obtained by using different initial velocities (randomly selected from a Boltzmann distribution). To generate amorphous silica slabs these systems were cooled to 298 K by ramping the temperature in the same NP_zAT ensemble at a cooling rate of 1 K/ps. All simulations were carried out using a Berendsen thermostat[40] with a damping constant of 1 ps and bulk modulus of 360,000 atm to control the temperature. The

pressure is maintained at 1.0 atm with a Berendsen barostat.[40] The slab is further equilibrated at room temperature for an additional 1 ns in an NP_zAT ensemble. An *ad hoc* procedure was used to functionalize the resulting amorphous silica slab surfaces. First, the undercoordinated atoms on the surface were functionalized by adding, in concert, an H atom to a singly coordinated O atom and an OH group to a three-coordinate Si atom. Second, H_2O molecules were added across the longest Si–O bonds on the slab surface until the desired hydroxyl density of 2 OH/nm^2 was obtained. The added atoms were placed to avoid any overlap with other surface atoms. Five different slabs obtained from this procedure were used in the present simulations. Finally, the functionalized slab is relaxed for 1 ns at 298 K in the same NP_zAT ensemble.

A slit pore was formed by placing a slab of liquid water between the two silica surfaces. Slit pores of pore widths 4 nm and 7 nm were generated by varying the width of the water layer; the precise dimension of each slit pore was determined by equilibration at constant pressure normal to the interface (P_z) in the NP_zAT ensemble for 7 ns followed by equilibration in the *NVT* (fixed volume *V*) ensemble. A single silanol on each surface was deprotonated by removing a H atom from the Si-O-H to generate an Si-O$^-$ moiety on each surface on both the top and bottom to represent a pore at pH = 6. Two Na^+ ions were added to the system, by replacing two water molecules, to keep the system charge neutral. The slit pore model systems were further equilibrated in a NP_zAT ensemble for 2 ns followed by further *NVT* equilibration for 1ns.

The SPC/E model was used to describe the water interactions.[3] The silica slab, except for the silanols, was kept frozen throughout the simulation. The silica-DDEC force field parameters were used for simulating silica systems. The force field parameters are given in the Supplementary Material. Intermolecular interactions were evaluated with a cutoff of 10.5 Å, and long-range electrostatic interactions were included using three-dimensional periodic boundary

conditions and the particle–particle particle-mesh (PPPM) solver[41, 42] with a tolerance of 10^{-4}. The SHAKE algorithm[43] was used for the water molecules and silanols.

For comparison, bulk water simulations were also carried out. A 1 ns trajectory of 343 water molecules in a cubic periodic box of length 21.725 Å (ρ= 1.000 g/cm^3) was propagated with a 1 fs timestep in the *NVT* ensemble at 298.15 K. The other simulation details were the same as those for the slit pores.

Calculation of Raman spectra and its temperature derivative

The Raman spectra were calculated using the empirical mapping approach proposed by Corcelli, Skinner, and co-workers.[44-46] The mapping approach is a quantum/classical description based on the empirical correlation, or "map," of the quantum mechanical vibrational properties with the electric field exerted by the molecular environment. The electric field is determined from the charges within the MD simulation. The frequencies are calculated using the map,

$$\omega_{01}^{(i)}(t) = 2762.6 - 3640.8\mathcal{E}_i(t) - 56641.0\mathcal{E}_i^2(t) \qquad (2)$$

Here $\omega_{01}^{(i)}(t)$ is the fundamental vibrational transition frequency of the *i*th OH at time *t* and $\mathcal{E}_i(t)$ is the electric field at the H atom of the *i*th OH along the OH bond direction from all atoms (water or silica) within a radius of 7.831 Å. An analogous map was used to determine the transition polarizability matrix elements needed to calculate the Raman spectrum.

The (isotropic) Raman line shape is calculated from the Fourier transform,

$$I(\omega) = \frac{1}{2\pi}\int_{-\infty}^{\infty} e^{-i\omega t}\phi_{iso}(t)\, dt \qquad (3)$$

where ϕ_{iso} is the polarizability response function,

$$\phi_{iso}(t) = \left\langle \alpha_{01}(0) \cdot \alpha_{01}(t)\, e^{i\int_0^t \omega_{01}(\tau)d\tau} \right\rangle e^{-|t|/2T_1} \qquad (4)$$

Here, T_1 is the vibrational energy relaxation time for which the experimental value of 1450 fs[7,8] was used, $\alpha_{01}(t)$ is the transition polarizability, and the brackets $\langle ... \rangle$ indicate a thermal average. It is within this thermal average that the temperature dependence of the Raman spectrum appears in two factors: The Boltzmann weighting factor in the average and the canonical partition function that normalizes it. Thus, the derivative of the $\alpha_{01}(t)$ with respect to $\beta = {}^{1}/_{k_B T}$,where k_B is the Boltzmann constant can be written as,[47]

$$\frac{d\phi_{iso}(t)}{d\beta} = -\phi_{iso,H}(t) = -\left\langle \delta H(0)\alpha_{01}(0) \cdot \alpha_{01}(t) e^{i\int_0^t \omega_{01}(\tau)d\tau} \right\rangle e^{-|t|/2T_1} \qquad (5)$$

Where $\delta H(0) = H(0) - \langle H(0) \rangle$; $\delta H(0)$ is the fluctuation of the total energy at t = 0, from its average value. This derivative can be calculated from a single temperature simulation. Using this temperature derivative internal energy contribution to the free energy of spectra can be obtained. Since the Raman spectrum is a dynamical quantity, it is not possible to rigorously calculate an internal energy, but one can define an *effective* internal energy,[47]

$$\Delta U_{Raman} = -\left(\frac{\partial \ln I(\omega)}{\partial \beta}\right) = \frac{I_H(\omega)}{I(\omega)} \qquad (6)$$

This internal energy profile represents the change in energy associated with changing the OH frequency, which does not require the breaking of the H-bond.[47-49] The calculated effective internal energy enables the prediction of the Raman spectra as a function of temperature using the simulated room temperature spectrum. Specifically, using a van't Hoff approximation it can be shown that,

$$I_{pred}(\omega;T_b) = \frac{I(\omega;T_a)e^{-(\beta_b - \beta_a)\Delta U_{Raman}(\omega)}}{\int_0^\infty P(\omega;T_a)e^{-(\beta_b - \beta_a)\Delta U(\omega)d\omega}} \qquad (7)$$

where T_a is the simulated temperature and T_b is the temperature at which the Raman spectrum is predicted. The denominator accounts for the fact that the van't Hoff factor is not norm-conserving and here $P(\omega;T_a)$ is the vibrational frequency distribution at temperature T_a and $\Delta U(\omega)$ is the frequency distribution internal energy as a function of frequency.

Results

Raman spectroscopy of bulk and nanoconfined HOD/H_2O solutions

Raman spectra normalized by the CH stretch band intensity for bulk and nanoconfined HOD/H_2O solutions are shown in Figure 1a-c. In agreement with the previous studies of bulk HOD/H_2O solutions,[15] with increasing temperature the OD lines are shifting to higher wavenumbers, and their normalized intensities are decreasing due to the weakening and breaking of H-bonds. In the following discussion we use "wavenumber" and "frequency" interchangeably because a wavenumber in cm^{-1} can be converted to a frequency in GHz by multiplying by 29.9792458. For bulk HOD/H_2O solutions (Fig. 1a) the blueshift is ~29 cm^{-1} based on the position of the most intense line centered at 2537 cm^{-1} at room temperature (273 K) and moves to 2566 cm^{-1} when temperature is increased to 85 °C (358 K). Similarly, a ~33 cm^{-1} blueshift with increasing temperature is also observed for the nanoconfined HOD/H_2O (Fig. 1b,c), with the overall normalized intensity slightly lower than for the bulk solution, because a part of the volume sampled with the Raman laser is occupied by SiO_2 solid. The corresponding simulated spectra are shown in Fig.1d-f for HOD/H_2O in the bulk liquid and in 4 and 7 nm slit pores. They mirror the behavior of the measured spectra, with a blueshift in the peak position of 30.625 cm^{-1} for the bulk case, and 32.575 cm^{-1} and 32.495 cm^{-1} for the 4 and 7 nm pores, respectively. In addition, as the temperature increases, the peak intensity is reduced in all three cases, but more significantly for bulk HOD/H_2O than for confined water.

In Figure 2 we summarize potential contributions to the broad OD stretch spectral region: low-frequency (low wavenumber) contribution to the spectrum at ~2440 cm^{-1} at room temperature is assigned to HOD molecules with strong H-bonds,[50] accepting H-bond from Si–OH surface groups and donating H-bonds to the HOD molecules further from the surface.[15, 51] The highest frequency spectral region at 2650 cm^{-1} at room temperature is assigned to HOD molecules that have weak/transiently broken H-bonds. The intermediate spectral regions are composed of the oscillations from HOD molecules with <4 H-bonds and other transient H-bonding structures.

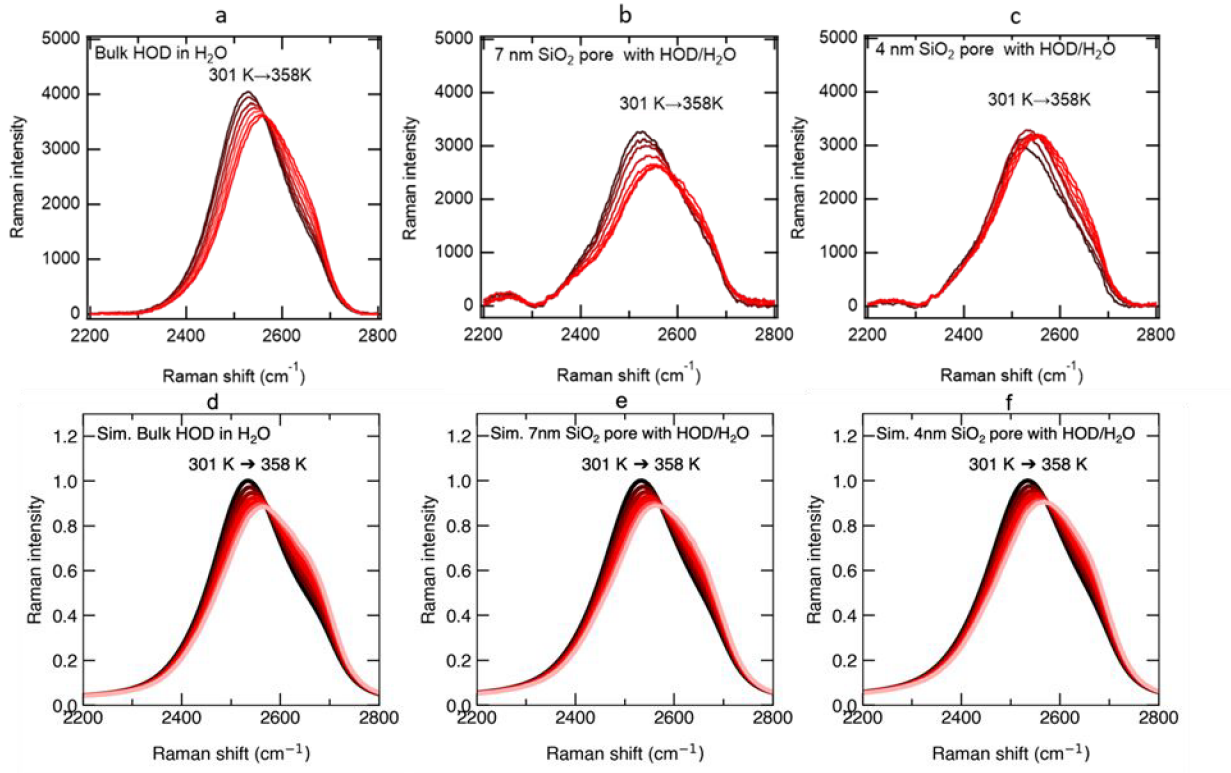

Figure 1. Measured (a-c) and simulated (d-f) Raman spectra of dilute HOD/H_2O as a function of temperature; (a),(d) bulk HOD/H_2O phase; (b),(e) HOD/H_2O nanoconfined in 7 nm SiO_2 pores; (c),(f) HOD/H_2O nanoconfined in 4 nm SiO_2 pores. The non-monotone changes in the Raman intensity in panel (c) are due to measurement uncertainty. Intensities decrease and characteristic lines shift to higher frequencies (blueshift) with increasing temperature. The measured Raman spectra are normalized by CH stretch band intensity, which is insensitive to temperature; the simulated spectra are normalized to a maximum of one at 298 K.

The simulated Raman spectrum can be decomposed into the contributions from OD groups in water with different numbers of H-bonds. In practice, this is done by separating the contributions based on the H-bond status of the molecule containing the OD group at *t=0* in the calculation of the polarizability response function, Eq. (4). An H-bond is determined by geometric criteria of $R_{O\cdots O} \leq 3.5$ Å, $r_{H\cdots O} \leq 2.45$ Å, and $\theta_{HO\cdots O} \leq 30°$. While the H-bond status may change over the time interval over which the response function is calculated, ϕ_{iso} decays rapidly. The results are shown in Fig. 2b for both 298 and 358 K. At room temperature, the dominant contribution to the spectrum comes from water molecules with 4 instantaneous H-bonds, with a moderate component from triply H-bonded molecules and small contributions from 2- and 5-coordinate waters. No significant population of water molecules with fewer than 2 H-bonds were observed in the MD simulations. Importantly, while the peak positions of the contributions increase in frequency as the number of H-bonds decreases, all the spectrum components overlap strongly. Thus, for example, OH groups from water molecules with 2, 3, 4, and 5 H-bonds all contribute to the total Raman signal at the frequency corresponding to the maximum in the cumulative peak. There is significant evidence from simulations that the presence of non-4-coordinated water molecules is associated with transient dynamics;[48] the 5-coordinate structures are transient ones important in H-bond exchange dynamics.[52] The results thus indicate that the higher frequency side of the spectrum is associated with molecules that involve weaker H-bonds and those undergoing transient H-bond breaks, while the lower frequencies arise from OD groups in molecules with strong H-bonds.

The decomposition of the spectrum at 358 K shows a decrease in the 4-coordinate water contributions and an increase in the 3-coordinate components when compared to the room temperature spectrum (Figure 2b). We cannot conclude from these simulations whether free OD

groups are present at these elevated temperatures, as would be expected when solutions are close to the liquid-vapor transition temperature, but these changes are consistent with a general weakening of the H-bonds within water and an increase in transiently broken H-bonds. This behavior underlies the blueshift of the spectrum with increasing temperature.

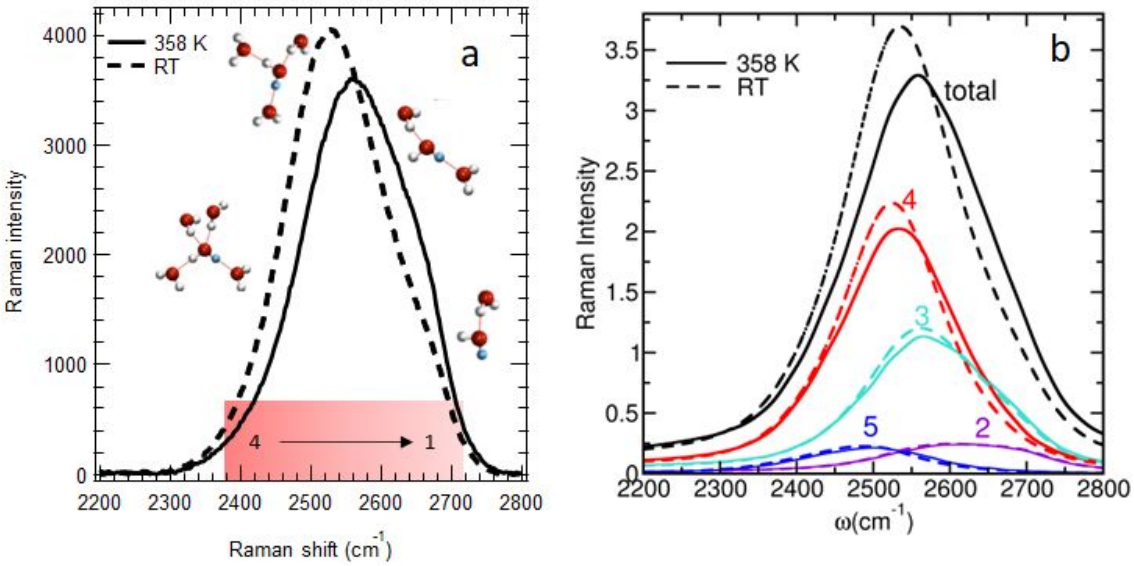

Figure 2. OD oscillator contributions in dilute HOD/H_2O to the cumulative OD stretch band signal measured by Raman spectroscopy and calculated using MD simulations. (a) Experiment: room temperature Raman spectra (RT, dashed line) and 358 K (solid line); Numbers and shaded areas indicate approximate positions for HOD oscillators with one to four H-bonds. Note, that not all possible H-bond arrangements are shown in the schematic; for the full discussion of H-bond configurations and corresponding Raman frequencies in neutral SiO_2 nanopores refer to Senanayake et al., 2021.[29] (b) MD-derived Raman spectra for cumulative signal at RT (dashed line) and 358K (solid line). Contributions from 2-, 3-, 4-, and 5-H-bonded HOD molecules are shown.

To compare Raman spectra for unconfined and nanoconfined HOD/H_2O solutions collected at the same temperature we show data that is normalized to the maximum intensity value in Figure 3. Here we consistently observe that the Raman intensity below 2440 cm^{-1} is higher for the HOD/H_2O nanoconfined in SiO_2 pores, compared to bulk solution. This observation may indicate: (*1*) an increased abundance of HOD molecules with strong H-bonds in the nanopore volume; and/or (*2*) an increased abundance of HOD molecules with strong H-bonds

within binding interfacial layer near SiO_2 surface, where HOD molecules are accepting H-bonds from the neutral Si–OH surface sites[51] or from nearby HOD molecules. Previous studies on unconfined SiO_2 surfaces showed that both weak and strong H-bonds may form in the interfacial regions, depending on the solution pH.[50, 51, 53] Alternatively, low frequency contributions may also arise from the Si–OD oscillators, since D can exchange for H at the silanol sites during the experiments. There is conflicting data in the literature with regards to assigning low-frequency spectral region for OH oscillator contributions.[54] Detailed MD investigation of the SiO–H stretch at two edge surfaces (010 and 110) of clay mineral pyrophyllite show that SiO–H frequency is sensitive to whether neighboring Si–OH sites form H-bonds with each other.[55] The non-H-bonded Si–OH moieties oscillate at ~ 3730-3800 cm^{-1} frequency, while for Si–OH groups that are H-bonded, maximum intensity shifts to the lower frequencies (3525; 3480; 3250 cm^{-1}, depending on the crystallographic orientation and the local environment around individual Si–OH oscillators).[55] Alternatively, the low-frequency line at ~ 3090 cm^{-1} recorded using infrared (IR) spectroscopy during H_2O adsorption onto germanium-based imogolite nanotubes was assigned to tetrahedral H_2O that is "firmly bound" to the Ge–OH surface groups inside nanotubes, since it was most pronounced at low relative humidity conditions, where H_2O was residing at the pore walls.[56] Contrary to the above, IR measurements of HOD in controlled pore glass indicate that H-bonding networks are weakened in near interfacial regions.[57]

The corresponding simulated Raman spectra are also shown in Fig. 3. They exhibit the same general features as the measured spectra. Namely, a broadening on the low frequency side of the spectrum upon confinement is observed while the rest of the spectrum is little changed. However, the simulations do not show the same increase in the difference between the bulk and confined spectra with increasing temperature. Previous simulations showed that the primary

frequency effect for OH (or OD) groups is a blueshift for those donating an H-bond to silica oxygen atoms, with the frequency distribution for OH groups more than ~5 Å from the silica surface nearly identical to that for the bulk.[29] The fact that the simulations do not reproduce the experimental temperature dependence in the low-frequency spectral region suggests the SPC/E model may underestimate the spectral diffusion activation energy.

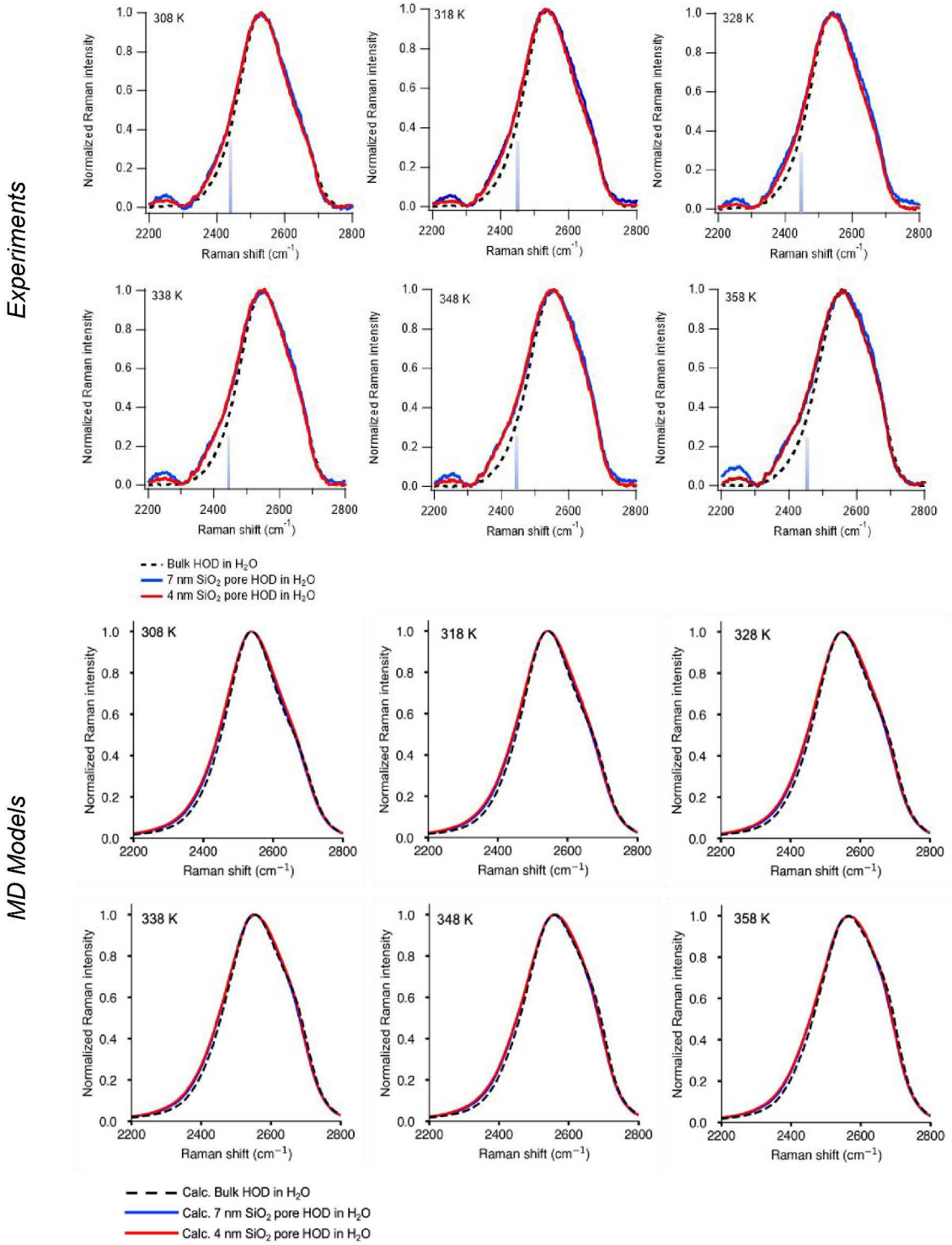

Figure 3. Raman spectra at different temperatures (308 K, 318 K, 328 K, 338 K, 348 K, and 358 K) for bulk HOD/H_2O (dashed line) and HOD/H_2O in SiO_2 with 4 nm (red) and 7 nm (blue) pores. Top six panels are experimental measurements, and bottom six panels are corresponding MD simulation results.

To determine the origin of the enhanced Raman scattering at 2400 cm^{-1} in our SiO_2 samples, we collected spectra from "dry" 4 nm SiO_2. Following the exposure to HOD/H_2O solution, SiO_2 sample was dried at ambient conditions, where some residual adsorbed HOD/H_2O would remain on the surface, and a Raman spectrum was collected. Then, the same sample was dried over-night at 200 °C (473 K) in a furnace. The duration and heating temperature were selected based on our DVS H_2O sorption measurements, that indicated that even at 0% RH some amount of adsorbed H_2O remains on the SiO_2 surfaces earlier exposed to water. To remove this residual H_2O, a porous sample requires heating at 200 °C for 24 hours. The Raman spectra collected after these two types of drying protocols are shown in Figure 4. It is apparent, that the intensity of the ~2400 cm^{-1} line for RT-dried sample is measurable and therefore it contributes to the overall spectra in Figure 3 (RT HOD/H_2O spectrum is shown for comparison). For the sample that was dried at 200 °C the intensity at ~2400 cm^{-1} vanishes. Therefore, we conclude that the observed enhanced signal in the low frequency range in our Raman measurements from nanoconfined solutions arises due to the HOD molecules with strong H-bonds within binding interfacial layer near SiO_2 surfaces. Earlier studies show that at SiO_2 surfaces both strong and weak H-bonds may form, depending whether O atoms of H_2O molecules point to or away from the surface.[51, 53] In the case when HOD accepts H-bonds from Si–OH groups, H-bonds are stronger compared to bulk solution, and when HOD donates H-bonds to the de-protonated Si-O^- group, the resulting H-bonds are weaker.[51] Therefore, here we report evidence that nanoconfinement promotes H-bonding interactions in near-interfacial regions, likely because HOD accepts H-bonds from Si–OH groups. While we cannot measure pH in these nanopores directly, earlier work shows that protons may accumulate in SiO_2 nanopores with negative surface charge.[8] If proton accumulation is taking place in our nanopores, a larger portion of the

surface Si–OH sites would be protonated, compared to unconfined SiO_2 with the similar Si–OH surface densities; therefore, there would be a larger availability of the H-bond donor sites on the surface that are capable of strong H-bonding with HOD molecules. We also anticipate that since Si–OH density of our surfaces is low at ~ 2 –OH nm^{-2}, it is possible that near-interfacial water molecules may form strong H-bonds with each other, since this water would experience surface-induced structuring. This hypothesis needs to be addressed in future studies.

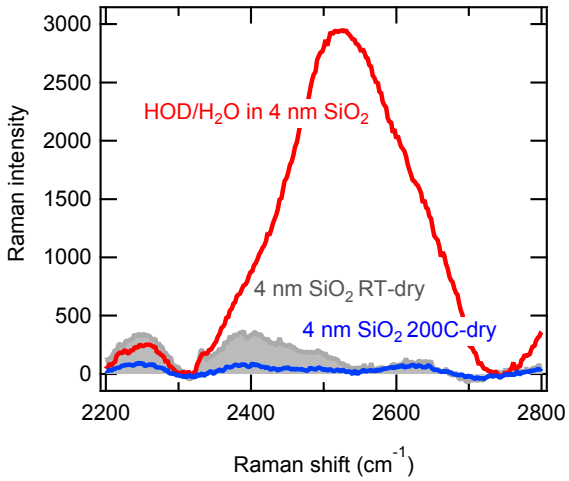

Figure 4. Raman spectra of dilute HOD/H_2O confined in 4 nm SiO_2 pore, collected at RT (red); the same 4 nm SiO_2 sample after it was dried overnight at ambient conditions; H_2O surface coverage is 0.009 mmol H_2O per m^2 (RT, ~30% RH) (gray); and the same 4 nm SiO_2 sample after it was dried overnight and kept at 200 °C during measurement to prevent re-adsorption of atmospheric water (blue).

In the IR spectroscopy investigation of nanoconfined polypropylene glycols (PPG) confined in silica with 4 nm pores, H-bonding strength between the PPG-OH groups increased under nanoconfinement, as evidenced by ~ 14 cm^{-1} redshift of the OH stretching mode of PPG-OH molecules.[58] In the same study, the lowest frequency OH stretching mode (3198-3026 cm^{-1}) was assigned to PPG molecules that are adsorbed and form H-bonds with the SiO_2 surface.

Temperature-dependent H_2O adsorption in SiO_2 nanopores

The difference between the unconfined and confined HOD/H_2O spectra in the <2440 cm^{-1} region becomes more pronounced with increasing temperature (Figure 3). To understand the nanoconfinement effects on the energetics of H_2O interactions with SiO_2 surfaces, we quantified

thermodynamics of H_2O adsorption onto non-confined and nanoconfined SiO_2 surfaces. H-bonding is the primary mode of interaction between H_2O and SiO_2; therefore enthalpy (ΔH_{ads}), entropy (ΔS_{ads}), and free energy (ΔG_{ads}) values determined from H_2O sorption measurements can indirectly indicate H-bond strengthening/weakening under nanoconfinement. Here we performed H_2O adsorption experiments at controlled temperatures (Figure 5). To obtain ΔH_{ads}, ΔS_{ads} and ΔG_{ads} values for H_2O adsorption onto non-porous SiO_2 and SiO_2 with 4 nm and 7 nm pores, we plotted $\ln(K_d)$ vs. $1/T$ and $\ln(K_L)$ vs $1/T$ values to calculate energetic parameters using the van't Hoff equation. Our analysis shows that in the 0-10 RH% range, Langmuir adsorption model does not fully capture H_2O adsorption behavior, and as a result the $\ln(K_L)$ vs. $1/T$ plots have poor linearity, despite clear temperature-dependency in adsorption isotherms for porous SiO_2 (Figure 5). Therefore, to calculate thermodynamic parameters we used K_d equilibrium constant values, and $\ln K_d$ vs.$1/T$ plots for porous SiO_2 have R^2 values of 0.9-1 for porous materials. The $\ln K_d$ vs.$1/T$ plot for non-porous SiO_2 is flat, with slope value close to zero (SI, Fig. S4), and therefore, ΔH_{ads} value is positive, due to the uncertainty in the data with weak temperature-dependence. The summary of the measured thermodynamic values derived from measured K_d values is shown in Table 1. The amount of adsorbed H_2O decreased with increasing temperature for porous SiO_2 materials, indicating an exothermic reaction. For non-porous SiO_2, the temperature-dependence for H_2O adsorption was insignificant. Progressively more negative ΔH_{ads} values for porous SiO_2 indicate that nanoconfinement makes H_2O adsorption and H-bonding with SiO_2 surface more exothermic; while negative ΔS_{ads} indicates that entropy decreases (system becomes more ordered, likely due to enhanced structure of H_2O at SiO_2 surfaces) during H_2O adsorption. Calculated ΔG_{ads} values are negative at room temperature, indicating that H_2O adsorption onto SiO_2 surfaces is spontaneous. Gibbs free energy for H_2O adsorption onto non-porous SiO_2 is the

highest (–2.0 kJ·mol^{-1}), therefore it is least favorable among the examined SiO_2 surfaces, while nanoconfinement decreases ΔG_{ads} to –2.7 and –3.5 kJ·mol^{-1}, making H_2O adsorption more favorable within SiO_2 nanopores. The ΔG_{ads} increase of –0.8 kJ·mol^{-1} corresponds to an increase of ~5% in the H-bond strength when pore diameter decreases from 7 nm to 4 nm, since H-bond at room temperature is ~ 4 kcal·mol^{-1}, or 16.7 kJ·mol^{-1}. Additionally, H_2O adsorption inside SiO_2 nanopores is much more exothermic (–6.0 to –9.5 kJ·mol^{-1}), when compared to unconfined SiO_2 surface (+0.5 kJ·mol^{-1}). When 4 nm and 7 nm pore diameters are compared, enthalpy, entropy and Gibbs free energy of H_2O adsorption become more negative with decreasing pore diameter. Therefore, nanoconfinement favors stronger H-bonding interactions at the SiO_2-H_2O interface.

The conceptual view of H_2O vapor sorption includes several approximately simultaneous reactions: (*1*) H_2O adsorbs and donates H-bonds to siloxide surface sites; (*2*) H_2O adsorbs and accepts H-bonds from protonated silanol surface sites; (*3*) H_2O adsorbs and donates H-bonds to de-protonated silanol surface sites; and (*4*) H-bonds are forming between H_2O molecules within binding interfacial H_2O layers. Here we consider H-bonding in liquid water exothermic because H-bonds are favored at lower temperature. If we assume that H_2O sorption and H-bond formation with siloxide, and protonated/de-protonated silanols are energetically equivalent between unconfined SiO_2 surfaces and SiO_2 surfaces inside nanopores, this will mean that H-bonding between H_2O molecules in the binding interfacial regions has more negative ΔH values inside nanopores when compared to H-bonding in near-interfacial regions on unconfined SiO_2 surface.

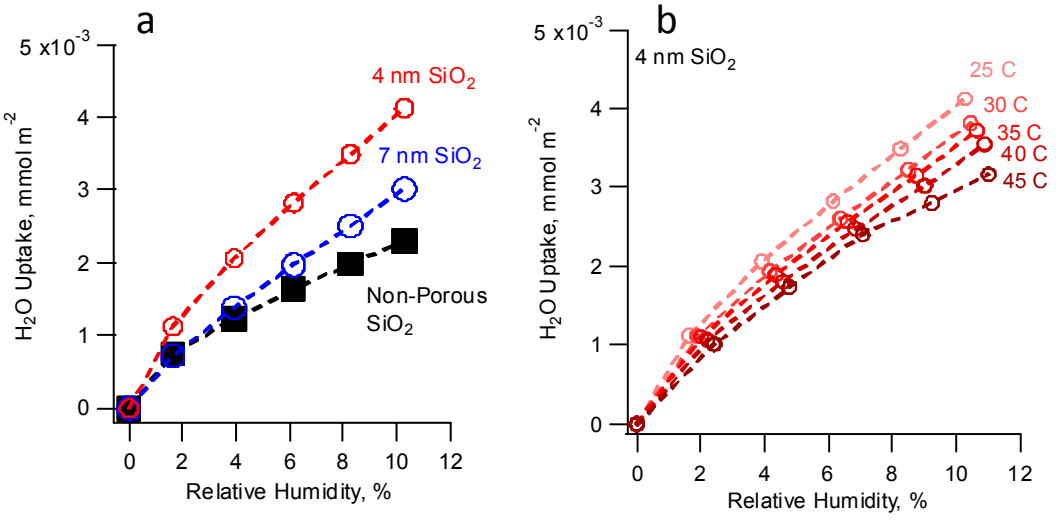

Figure 5. (a) H_2O adsorption onto porous and non-porous SiO_2 at room temperature (298K); and (b) temperature-dependent H_2O adsorption onto 4 nm SiO_2. Adsorption decreases with increasing temperature, indicating exothermic reaction in nanopores. For non-porous SiO_2, H_2O adsorption is nearly independent of temperature.

Table 1. Thermodynamic parameters for H_2O adsorption onto non-porous SiO_2 and SiO_2 with 4 nm and 7 nm pores determined using H_2O vapor sorption isotherms in a temperature range 25-45 °C (298-318 K).

	ΔH_{ads}, kJ·mol^{-1}	ΔS_{ads}, kJ·mol^{-1}K	ΔG_{ads} at 25C, kJ·mol^{-1}
Non-porous SiO_2	+0.5	+0.01	–2.0
7 nm SiO_2	–6.0	–0.01	–2.7
4 nm SiO_2	–9.5	–0.02	–3.5

H-bond energy in nanoconfined HOD/H_2O and implications for liquid-vapor phase boundary in nanoconfined water

To assess H-bond energetics across the entire nanopore volume, we used a method earlier developed for bulk HOD/H_2O solutions, and detailed in the Methods section.[15] The energy differences between the OD oscillator states at a reference frequency (ν_0) and at incidental frequency (ν) are shown in Figure 6. The resulting effective internal energy of an OD bond (in K) is plotted as a function of its vibrational frequency (Raman shift) and is compared between

bulk and nanoconfined HOD/H_2O solutions. We obtain excellent agreement between our data for bulk HOD/H_2O with that reported in the earlier publication (Ref [15]), despite using different instrumentation and materials. We find that the minimum in the effective internal energy of an OD bond occurs at different frequencies for bulk and nanoconfined solutions: 2440 cm^{-1} for bulk phase (consistent with Ref [15]), and 2465 cm^{-1} for nanoconfined solutions. Because the energy minimum shifts to a higher wavenumber (higher frequency) under nanoconfinement, this indicates that the mean bond length of the OD covalent bond in the nanopore volume (but not for the HOD/H_2O near SiO_2 surfaces) is shorter,[21] indicating that H-bonding interactions in the nanopore volume are weakened. Furthermore, the energy maxima for bulk solutions is higher than that for nanopores (Figure 6), indicating a smaller energetic cost to move to a higher frequency in nanoconfined solutions. In other words, it takes less energy to weaken H-bonds in nanopores, which may shift liquid-vapor transition temperatures to lower values.

The effective internal energy profiles obtained from MD simulations using Eq. (6) are shown in Fig. 5b. They show similar general behavior to that observed in the experimental results. Namely, the internal energy rises with frequency, indicating weakening of the OD H-bond. The minimum for unconfined and confined solutions is observed at a lower frequency, ~2480 cm^{-1} and contrary to experiments does not shift under nanoconfinement. The simulations underestimate the energy cost to change an OD frequency from its lowest internal energy value to that corresponding to a weakened, or transiently broken, H-bond (~9 kJ/mol compared to the measured value of 14.6 kJ/mol in bulk HOD/H_2O). However, they show the same reduction of this energy penalty with increasing confinement. Finally, the simulations do not show the experimentally observed shift in the internal energy minimum frequency upon confinement; this is likely related to the limited ability of confined solutions to expand (constant volume) in the

MD model, underestimating H-bond breaking and lowering of HOD density with increasing temperature.

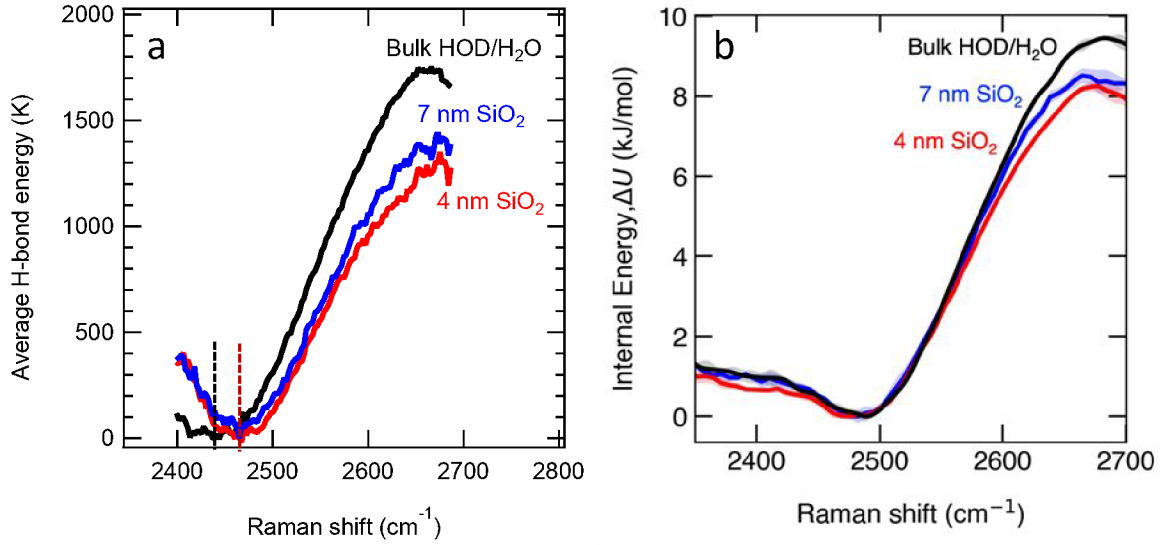

Figure 6. (a) The effective internal energy of an OD bond as a function of its vibrational frequency (in Kelvin) for dilute HOD/H_2O solutions, and for the same solutions confined in 7 nm and 4 nm SiO_2 pores. Each data point is the slope of the line extracted from $\ln[I(\nu,T)/I(\nu_0,T)]$ vs. $1/T$ plots (a total of 125 plots were made for each bulk HOD/H_2O, 4 nm and 7 nm pores); (b) MD-derived effective internal energy of OD bonds as a function of the fundamental vibrational frequency obtained from Eq. (6). Shaded regions indicate uncertainty in the internal energy values.

We show that the internal energy required to change the OD frequency in nanopore-confined water is decreased. This observation is consistent with earlier reports of a decrease in H_2O density when it is confined in SiO_2 nanopores.[5, 6] Decrease in H_2O density directly leads to a decrease in the number of H-bond donors/acceptors, lowering liquid-vapor transition temperature. The liquid-vapor line shifts towards vapor in carbon nanotubes[59] and nano-slits[60] and our data indicates that similar decrease in the liquid-vapor transition temperature (boiling point) may take place in SiO_2 nanopores. While our spectroscopic analysis cannot pinpoint the exact change is the vapor pressure for the liquid-vapor transition as a function of nanopore diameter, our spectroscopic data shows that it should be decreased in the nanopore volume (but

not in the binding interfacial layers), similar to a decrease in the liquid-ice transition temperature in nanopores.[6]

Environmental Implications

In this paper we quantified H-bond energetics and structures in dilute HOD/H_2O solutions confined in 7 nm and 4 nm SiO_2 pores using temperature-controlled Raman spectroscopy, dynamic H_2O vapor sorption measurements, and classical molecular dynamics simulations. When HOD/H_2O is confined, isolated OD group oscillations are enhanced in the low frequency region at ~2400 cm^{-1}, due to the strong H-bonding in HOD populations in the binding interfacial layer. The temperature-dependent H_2O vapor sorption measurements support this spectroscopic finding because enthalpy, entropy and Gibbs free energy of H_2O surface sorption become more negative with increasing nanoconfinement. As opposed to enhancing H-bonding interactions in the interfacial layer, in the nanopore volume away from the surfaces nanoconfinement weakens H-bonding strength assessed *via* vibrational frequency: the H-bond energy minima occurs at 2440 cm^{-1} for unconfined HOD/H_2O solutions and shifts to 2465 cm^{-1} inside SiO_2 nanopores. Therefore, we postulate the existence of two H_2O populations inside SiO_2 nanopores: (*1*) H_2O with strong H-bonds in the binding interfacial layer accepting H-bonds from the protonated Si–OH groups, and (*2*) H_2O in the center of SiO_2 nanopores, that has weakened H-bonds in comparison to bulk solutions. Both proposed water populations are affected by nanoconfinement-driven changes of the H-bonding structures and energetics, but in the opposite ways. Two-populations of water in nanopores (near-surface and “core” water) were also reported for imogolite,[56] zeolite,[61] and Vycor glass.[22] Furthermore, in imogolites H_2O forms strongly-bound interfacial layer with three H-bonds between H_2O molecules and imogolite surface.[62] The H-bond weakening in SiO_2 nanopores away from interfacial regions may lower the H_2O liquid-

vapor phase transition temperature, consistent with observations for carbon nanotubes and freezing point depression in silica nanopores. In agreement with the present finding that H-bonding interactions are weakened in the SiO_2 nanopore body (and de-solvation costs are decreased), we recently reported that for formic and acetic acids the de-protonation reaction equilibrium shifts towards the protonated forms (their pK_a values increase by ~ 0.2 units) when these acids are confined within the 4 nm SiO_2 pores.[63] Understanding molecular details of H-bonding networks in nanopores is important since they define aqueous species solvation energetics, the reactivities of nanoconfined surfaces, and phase boundaries of nanoconfined fluids.

Supporting information

- Example linear plots for Raman intensity ratios used to construct internal energy plots in Fig 3.;
- Comparison of the published[15] data on bulk HOD/H_2O solutions with our new data on bulk solutions showing excellent agreement of the frequency-dependent internal OD energies;
- Internal energy plots with ν_o = 2440 cm^{-1} an ν_o=2465 cm^{-1} reference frequencies for comparison;
- The lnK_d vs.1/T plots for porous and non-porous SiO_2;
- The proposed silica-DDEC force field charges and Lennard-Jones parameters.

References

(1) Castor-Villegas, V. M.; Guevara-Vela, J. M.; Vallejo Narvaez, W. E.; Martin Pendas, A.; Rocha-Rinza, T.; Fernández-Alarcón, A. On the strength of hydrogen bonding within water clusters on the coordination limit. *Journal of Computational Chemistry* **2020**, *41* (26), 2266-2277.
(2) Bulavin, L.; Gotsulskyi, V. Y.; Malomuzh, N.; Fisenko, A. Crucial role of water in the formation of basic properties of living matter. *Ukrainian Journal of Physics* **2020**, *65* (9), 794-794.
(3) Fumagalli, L.; Esfandiar, A.; Fabregas, R.; Hu, S.; Ares, P.; Janardanan, A.; Yang, Q.; Radha, B.; Taniguchi, T.; Watanabe, K. Anomalously low dielectric constant of confined water. *Science* **2018**, *360* (6395), 1339-1342.
(4) Varghese, S.; Kannam, S. K.; Hansen, J. S.; Sathian, S. P. Effect of hydrogen bonds on the dielectric properties of interfacial water. *Langmuir* **2019**, *35* (24), 8159-8166.
(5) Takei, T.; Mukasa, K.; Kofuji, M.; Fuji, M.; Watanabe, T.; Chikazawa, M.; Kanazawa, T. Changes in density and surface tension of water in silica pores. *Colloid and Polymer Science* **2000**, *278* (5), 475-480.
(6) Knight, A. W.; Kalugin, N. G.; Coker, E.; Ilgen, A. G. Water properties under nano-scale confinement. *Scientific reports* **2019**, *9* (1), 8246.
(7) Breynaert, E.; Houlleberghs, M.; Radhakrishnan, S.; Grübel, G.; Taulelle, F.; Martens, J. A. Water as a tuneable solvent: a perspective. *Chemical Society Reviews* **2020**, *49* (9), 2557-2569.
(8) Zhu, Y.; Derami, H. G.; Gupta, P.; Gupta, R.; Singamaneni, S.; Jun, Y.-S. Ionic surface propensity controls pH in nanopores. *Chem* **2022**.
(9) Gao, Z.; Giovambattista, N.; Sahin, O. Phase diagram of water confined by graphene. *Scientific reports* **2018**, *8* (1), 6228.
(10) Agrawal, K. V.; Shimizu, S.; Drahushuk, L. W.; Kilcoyne, D.; Strano, M. S. Observation of extreme phase transition temperatures of water confined inside isolated carbon nanotubes. *Nature nanotechnology* **2017**, *12* (3), 267-273.
(11) Ortiz-Young, D.; Chiu, H.-C.; Kim, S.; Voïtchovsky, K.; Riedo, E. The interplay between apparent viscosity and wettability in nanoconfined water. *Nature communications* **2013**, *4* (1), 2482.
(12) Murota, K.; Saito, T. Pore size effects on surface charges and interfacial electrostatics of mesoporous silicas. *Physical Chemistry Chemical Physics* **2022**, *24* (30), 18073-18082.
(13) Ilgen, A. G.; Leung, K.; Criscenti, L. J.; Greathouse, J. A. Adsorption at Nanoconfined Solid–Water Interfaces. *Annual Review of Physical Chemistry* **2023**, *74*, 169-191.
(14) Tsukahara, T.; Hibara, A.; Ikeda, Y.; Kitamori, T. NMR study of water molecules confined in extended nanospaces. *Angewandte Chemie International Edition* **2007**, *46* (7), 1180-1183.
(15) Hare, D.; Sorensen, C. Raman spectroscopic study of dilute HOD in liquid H2O in the temperature range− 31.5 to 160 C. *The Journal of chemical physics* **1990**, *93* (10), 6954-6961.
(16) Hare, D.; Sorensen, C. Interoscillator coupling effects on the OH stretching band of liquid water. *The Journal of chemical physics* **1992**, *96* (1), 13-22.
(17) Le Caër, S.; Pin, S.; Esnouf, S.; Raffy, Q.; Renault, J. P.; Brubach, J.-B.; Creff, G.; Roy, P. A trapped water network in nanoporous material: the role of interfaces. *Physical Chemistry Chemical Physics* **2011**, *13* (39), 17658-17666.
(18) Malfait, B.; Moréac, A.; Jani, A.; Lefort, R.; Huber, P.; Fröba, M.; Morineau, D. Structure of Water at Hydrophilic and Hydrophobic Interfaces: Raman Spectroscopy of Water Confined in Periodic Mesoporous (Organo) Silicas. *The Journal of Physical Chemistry C* **2022**, *126* (7), 3520-3531.
(19) Auer, B.; Skinner, J. Water: Hydrogen bonding and vibrational spectroscopy, in the bulk liquid and at the liquid/vapor interface. *Chemical physics letters* **2009**, *470* (1-3), 13-20.
(20) Perakis, F.; De Marco, L.; Shalit, A.; Tang, F.; Kann, Z. R.; Kühne, T. D.; Torre, R.; Bonn, M.; Nagata, Y. Vibrational spectroscopy and dynamics of water. *Chemical reviews* **2016**, *116* (13), 7590-7607.

(21) Boyer, M. A.; Marsalek, O.; Heindel, J. P.; Markland, T. E.; McCoy, A. B.; Xantheas, S. S. Beyond Badger's rule: The origins and generality of the structure–spectra relationship of aqueous hydrogen bonds. *The Journal of Physical Chemistry Letters* **2019**, *10* (5), 918-924.
(22) Gordillo, M.; Martı, J. Hydrogen bond structure of liquid water confined in nanotubes. *Chem. Phys. Lett.* **2000**, *329* (5-6), 341-345.
(23) Terpstra, P.; Combes, D.; Zwick, A. Effect of salts on dynamics of water: A Raman spectroscopy study. *The Journal of chemical physics* **1990**, *92* (1), 65-70.
(24) Smith, J. D.; Saykally, R. J.; Geissler, P. L. The effects of dissolved halide anions on hydrogen bonding in liquid water. *Journal of the American Chemical Society* **2007**, *129* (45), 13847-13856.
(25) Pezzotti, S.; Serva, A.; Sebastiani, F.; Brigiano, F. S.; Galimberti, D. R.; Potier, L.; Alfarano, S.; Schwaab, G.; Havenith, M.; Gaigeot, M.-P. Molecular Fingerprints of Hydrophobicity at Aqueous Interfaces from Theory and Vibrational Spectroscopies. *The Journal of Physical Chemistry Letters* **2021**, *12* (15), 3827-3836. DOI: 10.1021/acs.jpclett.1c00257.
(26) Rovere, M.; Ricci, M.; Vellati, D.; Bruni, F. A molecular dynamics simulation of water confined in a cylindrical SiO 2 pore. *The Journal of chemical physics* **1998**, *108* (23), 9859-9867.
(27) Hartnig, C.; Witschel, W.; Spohr, E.; Gallo, P.; Ricci, M. A.; Rovere, M. Modifications of the hydrogen bond network of liquid water in a cylindrical SiO2 pore. *Journal of Molecular Liquids* **2000**, *85* (1-2), 127-137.
(28) Laage, D.; Thompson, W. H. Reorientation dynamics of nanoconfined water: Power-law decay, hydrogen-bond jumps, and test of a two-state model. *The Journal of chemical physics* **2012**, *136* (4), 044513.
(29) Senanayake, H. S.; Greathouse, J. A.; Ilgen, A. G.; Thompson, W. H. Simulations of the IR and Raman spectra of water confined in amorphous silica slit pores. *The Journal of Chemical Physics* **2021**, *154* (10), 104503.
(30) Rieth, A. J.; Hunter, K. M.; Dincă, M.; Paesani, F. Hydrogen bonding structure of confined water templated by a metal-organic framework with open metal sites. *Nature communications* **2019**, *10* (1), 1-7.
(31) Medders, G. R.; Paesani, F. Water dynamics in metal–organic frameworks: Effects of heterogeneous confinement predicted by computational spectroscopy. *The Journal of Physical Chemistry Letters* **2014**, *5* (16), 2897-2902.
(32) Fogarty, A. C.; Duboué-Dijon, E.; Laage, D.; Thompson, W. H. Origins of the non-exponential reorientation dynamics of nanoconfined water. *The Journal of Chemical Physics* **2014**, *141* (18), 18C523.
(33) Yamada, S. A.; Hung, S. T.; Thompson, W. H.; Fayer, M. D. Effects of pore size on water dynamics in mesoporous silica. *The Journal of Chemical Physics* **2020**, *152* (15), 154704.
(34) Knight, A. W.; Tigges, A. B.; Ilgen, A. G. Adsorption of copper (II) on mesoporous silica: the effect of nano-scale confinement. *Geochemical Transactions* **2018**, *19*, 1-13.
(35) Knight, A. W.; Ilani-Kashkouli, P.; Harvey, J. A.; Greathouse, J. A.; Ho, T. A.; Kabengi, N.; Ilgen, A. G. Interfacial reactions of Cu (II) adsorption and hydrolysis driven by nano-scale confinement. *Environmental Science: Nano* **2020**, *7* (1), 68-80.
(36) Ilgen, A. G.; Kabengi, N.; Leung, K.; Ilani-Kashkouli, P.; Knight, A. W.; Loera, L. Defining silica–water interfacial chemistry under nanoconfinement using lanthanides. *Environmental Science: Nano* **2021**, *8* (2), 432-443.
(37) Venkateswarlu, K. Effect of temperature on the intensities of Raman lines. Part III. liquids. In *Proceedings of the Indian Academy of Sciences, Section A*, 1944; Indian Academy of Sciences: Vol. 19, pp 111-116.
(38) Thompson, A. P.; Aktulga, H. M.; Berger, R.; Bolintineanu, D. S.; Brown, W. M.; Crozier, P. S.; in 't Veld, P. J.; Kohlmeyer, A.; Moore, S. G.; Nguyen, T. D.; et al. LAMMPS - a flexible simulation tool for

particle-based materials modeling at the atomic, meso, and continuum scales. *Computer Physics Communications* **2022**, *271*, 108171. DOI: https://doi.org/10.1016/j.cpc.2021.108171.
(39) Wimalasiri, P. N.; Nguyen, N. P.; Senanayake, H. S.; Laird, B. B.; Thompson, W. H. Amorphous Silica Slab Models with Variable Surface Roughness and Silanol Density for Use in Simulations of Dynamics and Catalysis. *The Journal of Physical Chemistry C* **2021**, *125* (42), 23418-23434. DOI: 10.1021/acs.jpcc.1c06580.
(40) Berendsen, H. J. C.; Postma, J. P. M.; van Gunsteren, W. F.; DiNola, A.; Haak, J. R. Molecular dynamics with coupling to an external bath. *Journal Of Chemical Physics* **1984**, *81* (8), 3684-3690.
(41) Darden, T.; York, D.; Pedersen, L. Particle mesh Ewald: An N·log(N) method for Ewald sums in large systems. *The Journal of Chemical Physics* **1993**, *98* (12), 10089-10092. DOI: 10.1063/1.464397.
(42) Pollock, E. L.; Glosli, J. Comments on P3M, FMM, and the Ewald method for large periodic Coulombic systems. *Computer Physics Communications* **1996**, *95* (2), 93-110. DOI: https://doi.org/10.1016/0010-4655(96)00043-4.
(43) Ryckaert, J.-P.; Ciccotti, G.; Berendsen, H. J. C. Numerical integration of the cartesian equations of motion of a system with constraints: molecular dynamics of n-alkanes. *Journal of Computational Physics* **1977**, *23* (3), 327-341. DOI: Doi: 10.1016/0021-9991(77)90098-5.
(44) Corcelli, S. A.; Lawrence, C. P.; Skinner, J. L. Combined electronic structure/molecular dynamics approach for ultrafast infrared spectroscopy of dilute HOD in liquid H2O and D2O. *The Journal of Chemical Physics* **2004**, *120* (17), 8107-8117. DOI: 10.1063/1.1683072.
(45) Auer, B. M.; Skinner, J. L. IR and Raman spectra of liquid water: Theory and interpretation. *The Journal of Chemical Physics* **2008**, *128* (22), 224511. DOI: 10.1063/1.2925258.
(46) Gruenbaum, S. M.; Tainter, C. J.; Shi, L.; Ni, Y.; Skinner, J. L. Robustness of Frequency, Transition Dipole, and Coupling Maps for Water Vibrational Spectroscopy. *Journal of Chemical Theory and Computation* **2013**, *9* (7), 3109-3117. DOI: 10.1021/ct400292q.
(47) Piskulich, Z. A.; Thompson, W. H. Temperature Dependence of the Water Infrared Spectrum: Driving Forces, Isosbestic Points, and Predictions. *J. Phys. Chem. Lett.* **2020**, *11* (18), 7762-7768, Article. DOI: 10.1021/acs.jpclett.0c02301.
(48) Eaves, J. D.; Loparo, J. J.; Fecko, C. J.; Roberts, S. T.; Tokmakoff, A.; Geissler, P. L. Hydrogen bonds in liquid water are broken only fleetingly. *Proceedings of the National Academy of Sciences USA* **2005**, *102* (37), 13019-13020.
(49) Piskulich, Z. A.; Laage, D.; Thompson, W. H. On the role of hydrogen-bond exchanges in the spectral diffusion of water. *The Journal of Chemical Physics* **2021**, *154* (6), 064501. DOI: 10.1063/5.0041270.
(50) Eftekhari-Bafrooei, A.; Borguet, E. Effect of hydrogen-bond strength on the vibrational relaxation of interfacial water. *Journal of the American Chemical Society* **2010**, *132* (11), 3756-3761.
(51) Myalitsin, A.; Urashima, S.-H.; Nihonyanagi, S.; Yamaguchi, S.; Tahara, T. Water structure at the buried silica/aqueous interface studied by heterodyne-detected vibrational sum-frequency generation. *The Journal of Physical Chemistry C* **2016**, *120* (17), 9357-9363.
(52) Laage, D.; Hynes, J. T. On the Molecular Mechanism of Water Reorientation. *The Journal of Physical Chemistry B* **2008**, *112* (45), 14230-14242. DOI: 10.1021/jp805217u.
(53) Sovago, M.; Campen, R. K.; Bakker, H. J.; Bonn, M. Hydrogen bonding strength of interfacial water determined with surface sum-frequency generation. *Chemical Physics Letters* **2009**, *470* (1-3), 7-12.
(54) Huang, X. F.; Wang, Q.; Liu, X. X.; Yang, S. H.; Li, C. X.; Sun, G.; Pan, L. Q.; Lu, K. Q. Vibrational dynamics of water within mesoporous materials at different hydration levels during adsorption and desorption processes. *The Journal of Physical Chemistry C* **2009**, *113* (43), 18768-18771.
(55) Harvey, J. A.; Johnston, C. T.; Criscenti, L. J.; Greathouse, J. A. Distinguishing between bulk and edge hydroxyl vibrational properties of 2: 1 phyllosilicates via deuteration. *Chemical Communications* **2019**, *55* (24), 3453-3456.

(56) Liao, Y.-Y.; Picot, P.; Brubach, J.-B.; Roy, P.; Thill, A.; Le Caër, S. Water adsorption in single-and double-walled inorganic nanotubes. *The Journal of Physical Chemistry C* **2019**, *123* (32), 19768-19777.
(57) Musat, R.; Renault, J. P.; Candelaresi, M.; Palmer, D. J.; Le Caër, S.; Righini, R.; Pommeret, S. Finite size effects on hydrogen bonds in confined water. *Angewandte Chemie International Edition* **2008**, *47* (42), 8033-8035.
(58) Talik, A.; Tarnacka, M.; Geppert-Rybczyńska, M.; Hachuła, B.; Kaminski, K.; Paluch, M. Impact of confinement on the dynamics and H-bonding pattern in low-molecular weight poly (propylene glycols). *The Journal of Physical Chemistry C* **2020**, *124* (32), 17607-17621.
(59) Chaban, V. V.; Prezhdo, O. V. Water boiling inside carbon nanotubes: toward efficient drug release. *ACS nano* **2011**, *5* (7), 5647-5655.
(60) Ferguson, A. L.; Giovambattista, N.; Rossky, P. J.; Panagiotopoulos, A. Z.; Debenedetti, P. G. A computational investigation of the phase behavior and capillary sublimation of water confined between nanoscale hydrophobic plates. *The Journal of Chemical Physics* **2012**, *137* (14), 144501.
(61) Alabarse, F. G.; Baptiste, B.; Jiménez-Ruiz, M.; Coasne, B.; Haines, J.; Brubach, J.-B.; Roy, P.; Fischer, H. E.; Klotz, S.; Bove, L. E. Different Water Networks Confined in Unidirectional Hydrophilic Nanopores and Transitions with Temperature. *The Journal of Physical Chemistry C* **2021**, *125* (26), 14378-14393.
(62) Monet, G.; Paineau, E.; Chai, Z.; Amara, M. S.; Orecchini, A.; Jimenéz-Ruiz, M.; Ruiz-Caridad, A.; Fine, L.; Rouzière, S.; Liu, L.-M. Solid wetting-layers in inorganic nano-reactors: the water in imogolite nanotube case. *Nanoscale Advances* **2020**, *2* (5), 1869-1877.
(63) Sit, I. F., Bidemi T; Baldo, Anthony P; Leung, Kevin; Grassian, Vicki H; Ilgen, Anastasia G. Formic and acetic acid pKa values increase under nanoconfinement. *RSC Advances* **2023**, *13*, 23147–23157. DOI: 10.1039/d2ra07944e.